Space- and Time-Resolved Mapping of Ionic Dynamic and Electroresistive Phenomena in Lateral Devices

Evgheni Strelcov,[†,*] Stephen Jesse,[†] Yen-Lin Huang,[‡] Yung-Chun Teng,[‡] Ivan I. Kravchenko,[†] Ying-Hao Chu,[‡] and Sergei V. Kalinin[†,*]

[†]Center for Nanophase Materials Sciences, Oak Ridge National Laboratory, Oak Ridge, Tennessee 37831, United States and [‡]Department of Materials Science and Engineering, National Chiao Tung University, Hsinchu 30010, Taiwan

ABSTRACT A scanning probe microscopy-based technique for probing local ionic and electronic transport and their dynamic behavior on the 10 ms to 10 s scale is presented. The time-resolved Kelvin probe force microscopy (tr-KPFM) allows mapping of surface potential in both space and time domains, visualizing electronic and ionic charge dynamics and separating underlying processes based on their time responses. Here, tr-KPFM is employed to explore the interplay of the adsorbed surface ions and bulk oxygen vacancies and their role in the resistive switching in a Ca-substituted bismuth ferrite thin film.

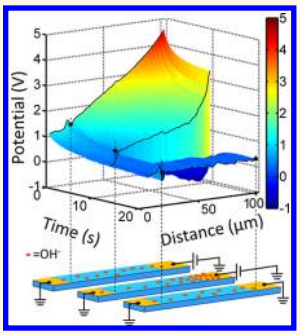

KEYWORDS: KPFM · ionic dynamics · Ca-BFO · surface potential distribution · oxygen vacancy

Electronic and ionic transport enables operation of numerous electrochemical devices including fuel cells, batteries, separators, and gas sensors.[1−6] Similarly, ionic phenomena undergird the functionality of emergent memristive and electroresistive memory and logic devices.[7−11] Much effort has been invested into the development of macroscopic strategies for separating the electronic and ionic responses, including electrochemical impedance spectroscopy and related methods.[12,13] However, in most, if not all, of these cases the transport is controlled by the nanoscale elements of a material's microstructure, including internal interfaces and grain boundaries in polycrystalline ceramics, interfaces in thin films, or conductive filaments in memristors. Typically, these elements possess a broad variability of properties, while only macroscopically averaged characterization is available experimentally. Therefore, probing *local* electronic and ionic transport phenomena is essential to understanding the fundamental mechanisms underpinning these devices. Beyond these applications, such information can facilitate understanding and mitigation of detrimental effects such as surface ionic leakage that plagues microelectronic and MEMS applications and can contribute to corrosion and degradation of metal electrodes under electrochemical conditions.

Understanding the *electronic* transport in lateral devices has necessitated the development of several current- (AFM- and STM-based potentiometry and nanoimpedance microscopies[14−18]) and force-sensitive scanning probe microscopy (SPM) techniques. These techniques can be considered nanoscale analogs of the classical methods of determining potential distribution, such as moving vibrating reed electrometry[19] and lateral electrode conductometry.[20−23] In particular, Kelvin probe force microscopy (KPFM)[24−29] and electrostatic force microscopy (EFM)[30,31] have emerged as powerful characterization methods and have been used in recent decades for studies of charge transport and accumulation in transistors,[32,33] solar and electrochemical cells,[30,34] microelectromechanical systems (MEMS),[35,36] gas sensors,[37−39] ferroelectric devices, and electroceramics.[40−42] This approach was further extended to map out linear and

* Address correspondence to strelcove@ornl.gov, sergei2@ornl.gov.

Received for review April 11, 2013 and accepted July 9, 2013.

Published online July 09, 2013
10.1021/nn4017873

nonlinear frequency-dependent transport, as implemented in the scanning impedance microscopy (SIM) and its nonlinear analogs.[29,43−46]

However, the fundamental limitation of these approaches is that only the *total* potential distribution induced by changes of the electronic and ionic distributions is probed. Moreover, these techniques usually do not distinguish between different mechanisms governing charge rearrangement, such as surface ions *versus* bulk ion diffusion, electronic *versus* ionic dymanics, potential distribution due to different types of electronic conductivity, *etc*. Notably, in most interpretations of the KPFM data on lateral devices, observed phenomena are attributed solely to electronic transport. At the same time, formation of charge haloes during KPFM experiments on lateral devices as observed by multiple authors[45,47,48] is clear evidence of surface ionic effects and suggests that the ionic and electronic subsystems have vastly different response times (Figure 1a). In fact, the significantly higher resolution observed in SIM as compared to KPFM of lateral devices, such as nanotubes,[49] is primarily related to the mitigation of the ionic contribution to the signal.[50] Recent work by Laboriante *et al.*[35] explored these effects using an electrode system with predefined symmetry, transforming the slow scan direction into the time dimension[47] by changing the electrode bias several times, while one image was captured.

These observations suggest that different transport phenomena (electronic *vs* ionic, surface *vs* bulk ionic, *etc*.) can be separated based on responses in the *time domain*. Here, we report a novel SPM technique—time-resolved Kelvin probe force microscopy (tr-KPFM)—that probes the time dynamics of the surface potential in both bias-on and bias-off states at each spatial location with a temporal resolution as low as 10 ms and achievable spatial resolution equal to that of KPFM.

RESULTS AND DISCUSSION

The system we have chosen to demonstrate the feasibility and advantages of the tr-KPFM technique is a Ca-substituted $BiFeO_3$ (CaBFO) thin film. A fascinating interplay between the ferroelectricity and ionic effects in this material has recently attracted much attention.[51,52] Pure bismuth ferrite epitaxial films exhibit a structural monoclinic−pseudotetragonal transition around 830 °C. Substitution of Bi^{3+} ions for the alkaline-earth ones (Ca^{2+}, Ba^{2+}) in this perovskite leads to a lowering of the transition temperature and, due to the highly stable oxidation state of Fe^{3+}, generation of oxygen vacancies as a means of charge compensation. At the Ca^{2+} content of about 10%, a local minimum of the transition temperature associated with a ferroelectric instability is reached.[51] The instability region is known for a prominent resistive switching behavior with a conductivity change of up to 3 orders of magnitude. The associated insulator−conductor transition is thought

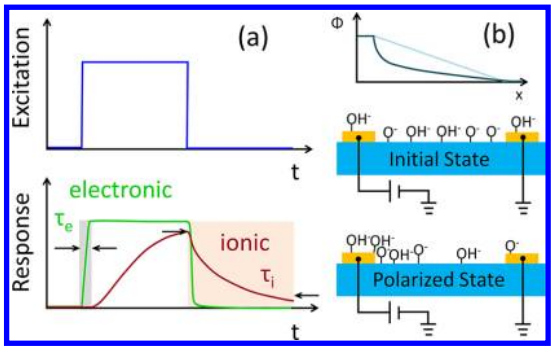

Figure 1. (a) Example of distinguishing between various response mechanisms: schematic depiction of the difference between the electronic and ionic response times triggered by an external step-like voltage excitation. (b) The initially linear surface potential profile between a biased and a grounded electrode curves down over time due to redistribution of the suface ions during the polarization process.

to be due to the redistribution of oxygen vacancies in CaBFO under the influence of an applied electric field.[51] Oxygen vacancies exist in a dynamic equilibrium with the electronic holes, and their motion should be linked to changes in the conductivity.

During switching, most of the 10% CaBFO film between a pair of lateral electrodes becomes highly p-conductive and depleted of oxygen vacancies, whereas a thin layer around the anode gains less in conductivity and turns into an n-type semiconductor.[53] However, this *bulk* picture can be expected to be altered by surface ionic and electronic dynamics (Figure 1b). Namely, in ambient, the oxide surfaces are universally covered by water layers and can contain physisorbed ionic species (compensating polar terminations, as is explored in ferroelectric materials[54−57]). These ions must create a space charge region near the film's surface, which depletes it of the main carriers and thus influences its conductivity. The thickness of the depletion region is on the order of the Debye length in CaBFO—quite comparable to the thin film's thickness. Formation of space charge region and modulation of the conduction channel through it constitutes the transduction function of the conductometric gas sensors[58] and can be expeted to affect electrochemical phenomena in thin films, as well. Under the applied electric field, the pre-existing charged species can redistribute, creating surface space charge layers (Figure 1b). Furthermore, the neutral molecules can split in the lateral electric fields, creating additional ionic carriers of both polarities. The question, then, arises whether the surface ions have any influence on the measured tr-KPFM data and on the insulator−conductor transition in this material. Here, we endeavor to investigate these behaviors in real space.

Schematics of the tr-KPFM, which is an extension of the scanning surface potential microscopy,[28] are shown in Figure 2a. Measurements are taken with a conventional AFM in dual pass mode a certain distance

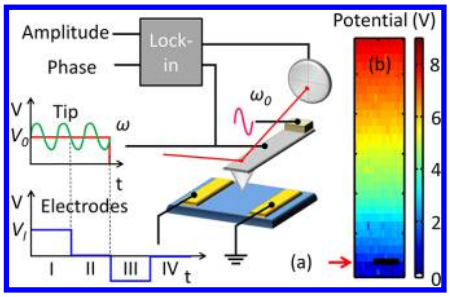

Figure 2. (a) Schematic of the tr-KPFM technique (description in the text); (b) time-averaged surface potential during polarization by a polarization pulse of 10 V applied between the lateral electrodes; scale bar is 10 μm; red arrow indicates position of the grounded electrode.

(z_0) above the surface on a predefined spatial grid. At each point of the grid, a four-step low-frequency probing voltage waveform is applied to the lateral electrodes, whereas the tip bias is modulated by a high-frequency AC signal. At step I, the device is polarized by a DC voltage V_1 applied between the electrodes, whereas $V_{tip} = V_0 + V_{ac} \times \cos(\omega t)$ waveform is applied to the tip. In order to avoid cross-talk, an AC frequency ω is chosen to be far away from the free resonance frequency of the cantilever ω_0, at which the tapping piezo mechanically excites the cantilever. During step II, the bias between the electrodes is brought to zero, allowing the material to relax, while the tip bias waveform is kept unchanged. As the surface potential at each grid point between the electrodes changes over time, so does the tip−surface force, which is reflected in the deflection signal and is detected by the lock-in. Steps II and III are used to restore the system to its initial state (*i.e.*, minimize charge accumulation and unwanted electrochemical processes) before moving to the next point of the grid, so that each measurement does not influence others. First, opposite bias $-V_1$ is applied between the electrodes (step II) and then the system is allowed to relax with both electrodes grounded (step III). As measurements are only taken during the first two steps, later the tip is kept grounded. Here, the duration of each step is chosen to be equal, albeit different pulse sequences and durations can be chosen depending on the nature of the physical phenomena under investigation.

The measured mechanical response of the cantilever can be quantified based on a simple electrostatic model. The periodic interaction force due to a capacitive coupling between the surface (at potential V_s) and tip (z meters away) is given by[26,28,59]

$$F_c(z,t) = \frac{1}{2}(V_{tip}(t) - V_s)^2 \frac{\partial C(z)}{\partial z}$$

Its first harmonic is

$$F_{c1\omega}(z) = \frac{\partial C(z)}{\partial z}(V_0 - V_s)V_{ac}$$

When the cantilever is held a fixed distance (z_0) above the surface, the deflection signal changes as a result of this periodic force, which is detected by the lock-in amplifier as the amplitude and phase of the signal:

$$A(\omega) = \frac{F_{c1\omega}}{m\sqrt{(\omega^2 - \omega_0^2)^2 + \omega^2\gamma^2}}$$

$$\tan(\theta) = \frac{\omega\gamma}{\omega^2 - \omega_0^2}$$

Here, m is the effective mass of the cantilever, ω_0 is its free mechanical oscillation frequency, and γ is the damping coefficient. Having recorded amplitude and phase of the signal, one can calculate the surface potential at each point of the grid as

$$V_s = V_0 - \frac{1}{f_{1\omega} \times \left.\frac{\partial C(z)}{\partial z}\right|_{z_0}} \times A = V_0 - K \cdot A\sin(\theta)$$

where K is the calibration coefficient and $f_{1\omega}$ is the transference function of the cantilever for the first harmonic.

Since the tip−surface capacitance and its dependence on z are generally unknown, K can be found by including part of the grounded lateral electrode in the scan. Then, the K calculated for the over-the-electrode grid points can be used for potential calibration for the rest of the grid. Potential calibration relies on the independence of the capacitance gradient on the tip position in the x−y plane (see Supporting Information). Note that, due to a stepwise height jump at the film−electrode interface, the V_s−A linear dependence assumption may fail and the potential may seem to jump, too. Recording several grid lines over the flat grounded electrode instead of just one line along the interface helps to eliminate this flaw and calibrate the surface potential correctly. Application of bias to the lateral electrodes may change the transference function of the cantilever due to its flexibility in the electrostatic field, in which case potential calibration should be done independently for bias-on and bias-off states (see Supporting Information).

We further note that determination of the local potential by KPFM is subject to several systematic corrections. First and foremost, the surface potential measured by KPFM differs from the absolute surface by a factor of the work function difference ($\Delta\chi$) of the surface and tip materials: $V_s = V_{abs} - \Delta\chi/e$ (e is the elementary charge).[60] Albeit, this difference generally does not exceed a fraction of the volt (for the ground state) and, hence, can be ignored here. For small bias measurements, the ground-state KPFM image can provide the required correction. Second, geometrical aspects of the tip−surface and cantilever−surface interactions may also influence the measured potential distribution.[61−63] However, these factors contribute to the spatial resolution. Finally, the feedback errors,

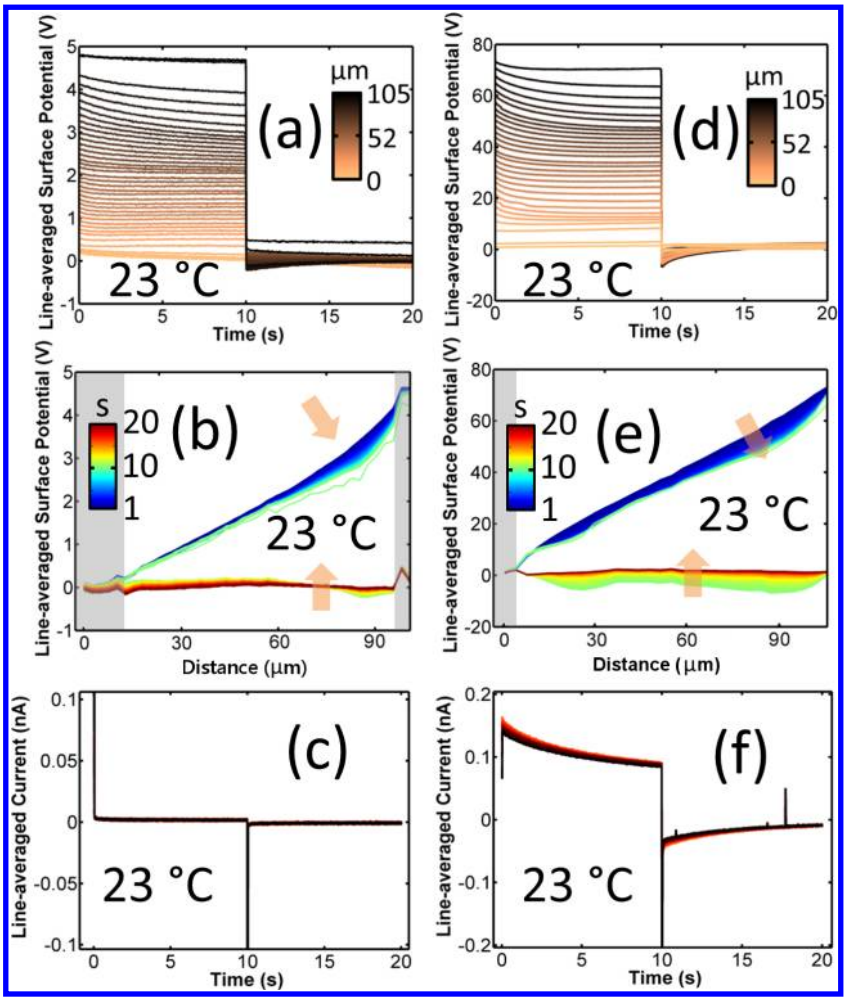

Figure 3. (a−c) Line-averaged surface potential *vs* time and position, and interelectrode current *vs* time as measured at room temperature with 5 V applied between the electrodes. (d−f) Same with 90 V applied to electrodes; gray rectangles show position of the lateral electrodes. Arrows and color bars in (b,e) indicate time sequence of the curves. Averaging was performed over spatial locations equidistant from the grounded electrode, which created a set of "lines", whose positions are indicated with the color bars in (a,d).

significant in KPFM,[56,64] do not affect the present implementation of tr-KPFM due to the open-loop detection scheme.

As an example of the surface mapping ability of the technique, Figure 2b shows a time-averaged surface potential of a $20 \times 105\ \mu m^2$ area of CaBFO film during a polarization pulse of 10 V lasting 10 s. Lines below the red arrow (Figure 2b) of the 20×30 grid were recorded over the grounded electrode, whereas the topmost line was adjacent to the biased electrode. In this example, extension of the collected data deep into the time domain decreased the spatial resolution of tr-KPFM as compared to standard EFM or SKPM techniques but simultaneously provided much more information on the surface potential dynamics. However, spatial resolution of the tr-KPFM technique is not in principle inferior to that of EFM and SKPM, but rather is linked to the temporal resolution and the total time an experimentor would like to spend acquiring one image.

Behavior of the CaBFO film in response to the applied bias is summarized in Figure 3. When 5 V is applied between the electrodes at room temperature, the detected potential (averaged over the pixels equidistant from one of the electrodes) decays during 10 s from a maximal to a lower value, more so for the regions closer to the biased electrode (Figure 3a). Switching bias off leads to an instant drop of potential to values close to zero and a subsequent relaxation of the remaining component.

The space−time distribution of potential is shown in Figure 3b, where both electrodes are represented with a gray shading. Initially (top dark-blue curve), the potential distribution between the electrodes is almost linear (except for the Schottky barrier at the biased electrode), but by the end of the 10 s polarization period (top green curve), it becomes somewhat reduced close to the biased electrode and, thus, deviates from linearity. As soon as both electrodes are grounded, potential drops and remains unevenly distributed, being less than zero close to the formerly biased electrode (lower green curve). The next 10 s of relaxation linearizes the potential profile and brings it

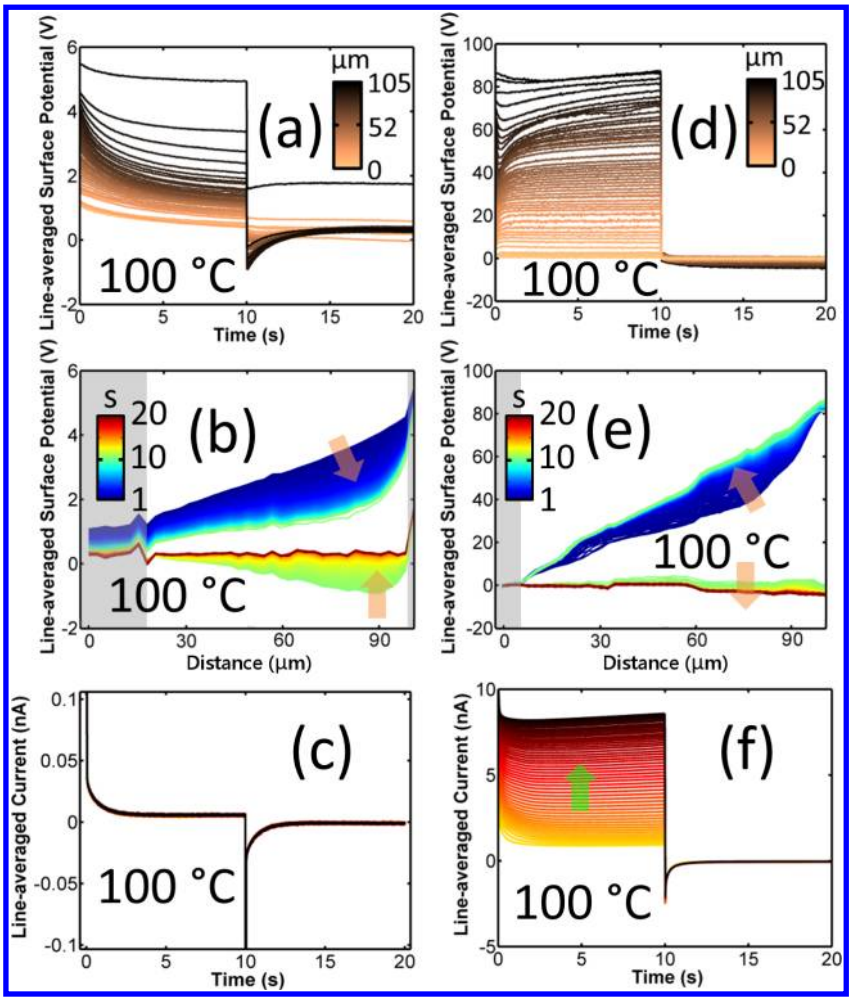

Figure 4. (a−c) Line-averaged surface potential *vs* time and position and interelectrode current *vs* time as measured at 100 °C with 5 V applied between the electrodes. (d−f) Same with 90 V applied to electrodes; gray rectangles show position of the lateral electrodes. Arrows and color bars in (b,e) indicate time sequence of the curves. Averaging was performed over spatial locations equidistant from the grounded electrode, which created a set of "lines", whose positions are indicated with the colorbars in (a) and (d).

almost to zero all over the sample. The peach arrows in Figure 3 indicate the time progression of the curves (in addition to the color-coding of the curves themselves). Note that Figure 3a,b shows two ways of presenting the same data. The nonlinear distribution of potential at the end of the polarization period indicated possible accumulation of negative charges in the vicinity of the positively biased electrode, which is also seen in the same region as a negative potential dip in the beginning of relaxation. These charges may be the oxygen vacancies of the bulk or the surface ions (hydroxyl groups, oxygen ions, or impurity ions left after photolithography). Since the motion of oxygen vacancies must bring about changes in the conductivity in CaBFO, whereas redistribution of the surface charges may not necessarily do so, and the current between the electrodes does not change (Figure 3c), we are likely dealing with surface ion motion in this case of low temperature and low bias. Notably, formation of the remanent potential feature only at one of the electrodes suggests the polarization of the existing ionic subsystem (*e.g.*, mobile part of the surface double layers).

Increasing interelectrode bias to 90 V at room temperature leads to increased accumulation of the opposite ions, while not changing the overall behavior much. The linearity of the potential distribution is succeeded by its bending during the polarization, and later, the negative potential "pits" relax to flat zero (Figure 3d−f). However, in this case, ions presumably accumulate at both electrodes, and the polarization current is higher. The current remains transient (Figure 3f) and does not increase over time, as it would in the case of oxygen vacancy motion. Hence, we still attribute the observed phenomena to the surface ion dynamics; however, in this case, the electrochemical splitting of water molecules can be an integral part of the process, resulting in additional generation of mobile ions.

Increasing temperature (*e.g.*, to 100 °C, Figure 4a−c) but keeping the bias low significantly enhances kinetics of the polarization and relaxation processes. Faster polarization means a larger amount of accumulated

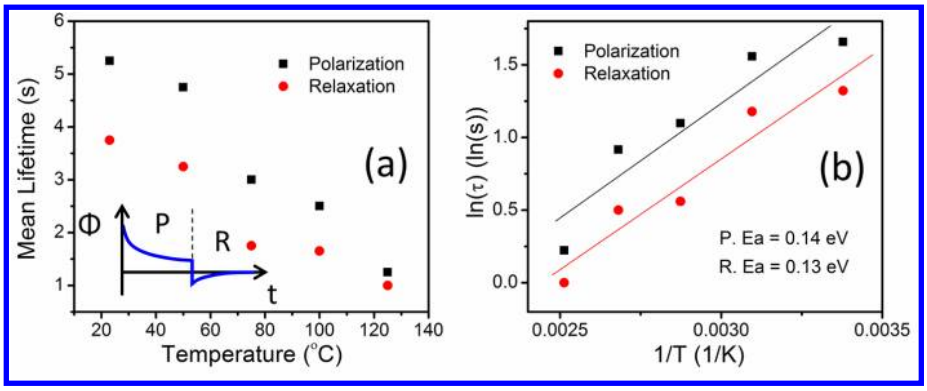

Figure 5. (a) Averaged mean lifetime of the surface potential decay at 5 V bias as a function of temperature. (b) Arrhenius plot of the averaged mean lifetime. Inset in (a) defines the polarization (*P*) and relaxation (*R*) periods.

ions and higher polarization current (Figure 4c) in the same 10 s polarization period. Thus, again, the potential distribution in these conditions is presumably governed by the surface ions rather than oxygen vacancies. Note that at low biases surface charges again pile up only by the biased electrode. We speculate that this behavior might be due to the splitting of the adsorbed water molecules in the high electric field. Thus, at high biases, in addition to the accumulation of negative surface ions at the positive electrode, some negative ions are generated at the grounded electrode, which serves as a source of electrons:

$$H_2O(s) + e^- \rightarrow H_2\uparrow + O^-(s)$$

Finally, high temperature and high bias conditions trigger the oxygen vacancy dynamics in addition to the surface charges motion, and a complicated potential distribution ensues (Figure 4d–f). Within the first tenth of a second from the application of bias, the initially linear distribution acquires an S-shape, indicating a very fast separation of opposite charges that build up by the electrodes and give rise to a fast-decaying current. However, during the next 9.9 s, the potential–distance curves slowly linearize again, and this process is accompanied by a gradual increase in current, as clearly visible in the black curve of Figure 4f.

This behavior must be explained by taking into account all three kinds of the charged particles existing in the system: the surface ions, bulk oxygen vacancies, and electrons/electronic holes of the film. We propose the following qualitative model for explaining the observed phenomena. Under a high driving force and while being thermally activated, surface ions redistribute themselves first (due to higher mobility), followed by the oxygen vacancies. Water splitting may also play a role here by generating more negative surface ions. The pile-up of the negative ions is then compensated by the electronic holes that are not only more mobile at high temperature but also more abundant, as they are generated alongside the oxygen vacancies' shift. This leads to a straightening of the potential distribution. Relaxation only equilibrates the surface ions, as evidenced by the small, quickly fading current, whereas the oxygen vacancies do not relax much, shifting further and further after each measurement and increasing the film's conductivity. This is seen in the progressive rise of the background current in Figure 4f, as indicated with the arrow.

The relaxation data can further be quantified using a simple phenomenological model similarly to earlier studies of relaxation in piezoresponse force microscopy.[65−67] The potential decay over time can be fitted with the exponential law: $\Phi = A + B \cdot e^{-t/\tau}$, where Φ is the surface potential, A is the offset, B is the pre-exponential factor, and τ is the mean lifetime, which is inversely proportional to the diffusion coefficient of the surface ions.

Figure 5a displays temperature dependence of the mean lifetime averaged over half of the grid points (where the fitting was most successful) for data taken at 5 V bias. As seen, τ values for the polarization and relaxation processes are slightly different (due to the lower signal-to-noise ratio of the relaxation curve) and steadily decrease with increasing temperature. The Arrhenius plot gives the value of the activation energy as approximately 0.14 eV (Figure 5b), which is very close to the 0.12 eV of the proton diffusivity in water.[68,69] The diffusivity of the surface ions can be estimated as $D = d^2/\tau$, where d is the distance ions have diffused in τ seconds. Obviously, it should be on the order of the interelectrode distance. The calculated value of diffusivity ($\sim 2 \times 10^{-9}$ m^2/s) is close to the room temperature diffusivity of protons in water ($\sim 10^{-8}$ m^2/s). This serves as an additional indication of the surface, rather than bulk ionic dynamics at low biases.

These observations suggest that the tr-KPFM dynamics readily observed on CaBFO surface is predominantly controlled by the *surface* ionic dynamics and electrochemistry of water layers that can couple to the bulk conductance through electrochemical gating effects. While providing only negligible current, these effects dominate the potential dynamics. In order to extend these studies to probe the *bulk* insulator–conductor

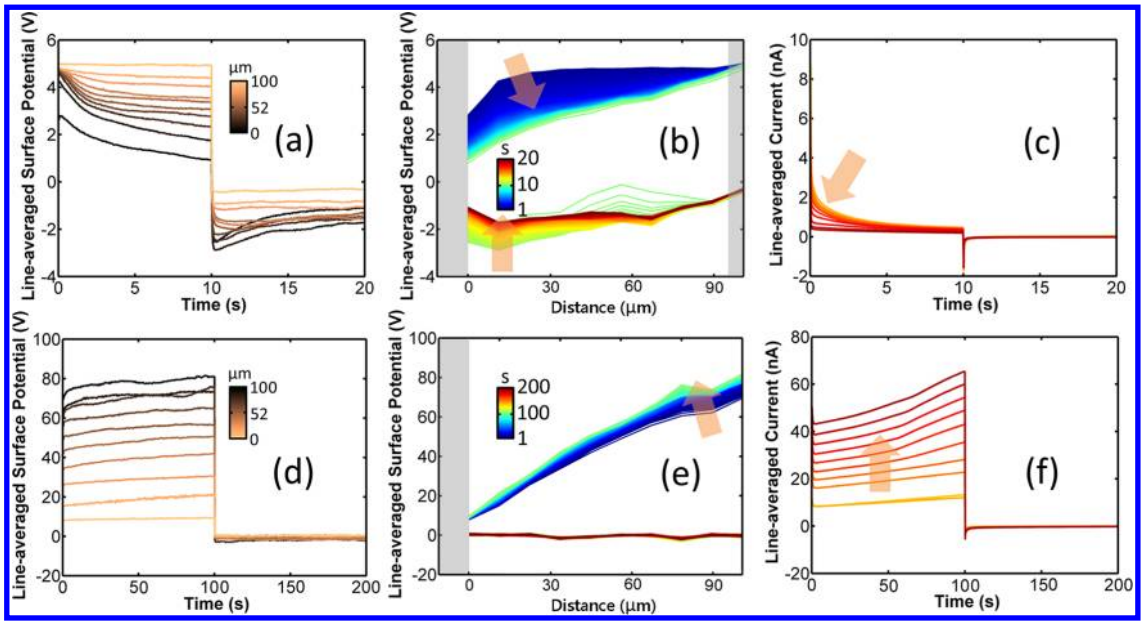

Figure 6. (a–c) Line-averaged surface potential *vs* time and position and interelectrode current *vs* time as measured at 100 °C with 5 V applied between the electrodes. (d–f) Same at 125 °C and 90 V bias. Arrows and colorbars in (b,e) indicate time sequence; gray rectangles represent electrodes. Averaging was performed over spatial locations equidistant from the grounded electrode, which created a set of "lines", whose positions are indicated with the colorbars in (a) and (d).

transition in CaBFO, one needs to either preactivate the sample or use longer polarization pulses. Both of these approaches were employed here, as discussed below.

Preactivation was done by biasing the electrodes with 90 V at 100 °C for *ca.* 40 min until current increased from 0.9 to 70 nA. The tr-KPFM imaging was started immediately after preactivation and showed that initially most of the film acquired the same potential as the biased electrode, and most of the potential drop took place close to the grounded electrode, where the p-n junction must have formed by the shifted oxygen vacancy density (Figure 6b). When the bias is switched off, this region remains more negatively charged than the rest of the film, indicating accumulation of negative ions in it, which dissipate during the relaxation period. The potential distribution linearization during polarization is accompanied by a decrease in current (Figure 6c). Taking these facts together, the following explanation can be given. The application of bias redistributes negative surface ions, accumulating them not at the biased electrode but in the region of the highest potential, at the shortest distance from the grounded electrode, since all regions of the film farther away are equipotential with the biased electrode. As negative ions pile up in the p-n junction region, they attract and trap electronic holes that partly compensate their charge. As a result, potential in the p-n junction region decreases and overall potential distribution straightens up by the end of the polarization period. Hole trapping also leads to a decrease in current. Thus, the surface ionic dynamics may play a role here in the resistive switching, acting as an impeding thermodynamic factor.

Prolonged application of high bias at elevated temperatures does eventually lead to the resistive switching in CaBFO film. Figure 6d–f demonstrates potential and current evolution in the sample at 125 °C under 100 s 90 V polarization pulses. In this case, all surface ion dynamics is condensed into the first several seconds and is almost invisible in the 100 s time scale, whereas the much slower motion of oxygen vacancies gradually increases the potential and current. The potential distribution remains nearly linear and would presumably curve upward at later stages (in *ca.* 40 min) to finally reach the shape of the dark-blue line in Figure 6b. Interestingly, next to no relaxation is observed in this case since the conductive CaBFO film is electroneutral and any excess charge relaxes very fast.

We further extend these studies to explore local ionic dynamics as visualized in spatially resolved maps of the fitting coefficients. Figure 7b presents such maps for the polarization/relaxation process that occurred in pristine sample under 30 V during 10 s and at room temperature, and Figure 7a shows the same for 5 V polarization pulse at 100 °C. The offset simply shows spatial distribution of potential: it is linear during polarization for room temperature and curved for 100 °C (compare to Figure 4b, green line) but is close to zero during relaxation in both cases. The pre-exponential factor maps describe how much potential drop occurred locally over the given period of time. For room temperature data, they clearly show two extrema close to the electrodes, where most polarization and relaxation took place due to accumulation of negative surface ions. This is similar to what is shown in Figure 3e. The high-temperature pre-exponential

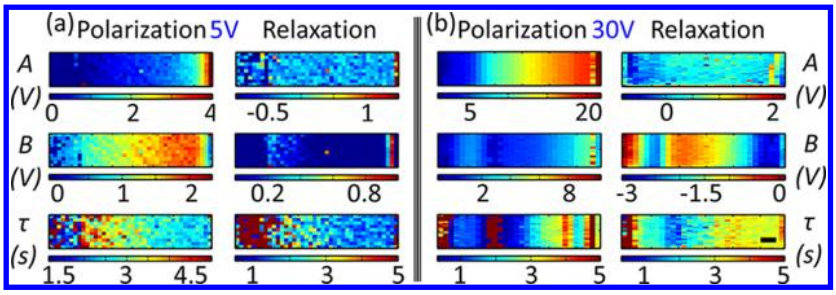

Figure 7. Fitting coefficients maps (spatial distribution of coefficients): *A* is the offset (in V), *B* is the pre-exponential factor (in V), and τ is the mean lifetime (in s) (a) for 5 V polarizing pulse at 100 °C, (b) for 30 V polarizing pulse at 23 °C. Several leftmost and rightmost lines of each map were recorded over the electrodes and stand out from the rest of the maps. Scale bar is 10 μm.

factor maps show maximal potential drop near the biased electrode. The mean lifetime maps also show some spatial variation but are only reliable in the regions of high potential drops, where the signal-to-noise ratio is highest and fitting is best. All in all, fitting coefficient maps condense the tr-KPFM data, reflecting both time and spatial information in one image and helping to extract useful information about the material behavior.

CONCLUSIONS AND OUTLOOK

In summary, we have presented a novel SPM-based technique for surface potential mapping in both space and time domains. The tr-KPFM allows one to probe ionic charge dynamcis even when corresponding currents are extremely small: on insulating and nearly insulating surfaces. Using it to investigate the ionic dynamics in CaBFO thin film, we have found that, at low biases and temperatures, all polarization/relaxation of the potential is due to surface charge motion, and only at higher temperatures, stronger electric fields, and longer time scales do oxygen vacancy dynamics begins to play the dominant role in conductivity. It is shown that in certain conditions surface ions may control the conductivity of the CaBFO thin film to a greater extent than the oxygen vacancies do.

Notably, this approach (a spatially resolved analog of the potentiostatic and galvanostatic intermittent titration techniques[70−72]) can differentiate the ionic from electronic dynamics in time domain and can be combined with the classical electrochemical impedance spectroscopy.[12,13] We further note that the use of the band excitation technique[73,74] will enhance resolution and sensitivity,[75] half-harmonic band excitation[76] detection can decouple potential and capacitive effects, and fast detection will allow measurements below the microsecond level, where the electronic response happens.[77] The tr-KPFM method can be used for probing the potential distribution in nano- and microelectronic devices, including adsorbed surface charge dynamics in conventional microelectronics (parasitic currents on SiO_2 and Si_3N_4 surfaces), surface *versus* bulk ionic dynamics in materials with the ion-controlled metal−insulator transition and resistive switching (Ca-BFO, as shown, NiO_x, *etc.*), and studies of gas interaction with solids, including spillover effects in catalysts and gas sensing in semiconductors.

METHODS

The studied sample was a 100 nm epitaxial film of 10% Ca-substituted $BiFeO_3$ grown on an insulating $SrTiO_3$ substrate. Lateral Au/Cr electrodes 100 μm wide, 3 mm long, and 200 nm thick were deposited 100 μm apart using a photolithographic mask and physical vapor deposition. Devices were fabricated by gluing the film to a chip carrier and performing wire bonding. Multimode AFM (Bruker) with a Nanonis (Specs) controller was used as a measuring platform. The bias application and signal recording was done by a computer *via* a National Instruments card controlled through Matlab and LabVIEW software. Two types of cantilevers with conductive coating tips were used for measurements: Budget Sensors (Cr/Pt coating, k = 3 N/m) and boron-doped diamond-coated (NT-MDT, k = 28−91 N/m). The former, being more flexible and sensitive, was used for measurements with biases lower than 10 V. When employing higher biases, the tr-KPFM grid was chosen outside the biased electrode, as accidental touching of the cantilever tip to it caused discharge and destruction of the tip. Current was measured with a Femto amplifier (DLPCA-200) connected in series with a 200 MΩ protective resistor. An external lock-in amplifier (SR844, Stanford Research) was used for signal processing, and a function generator (DS345, Stanford Research) applied AC waveform to the tip. Data processing was done using custom-written Matlab codes. Some of the outlier points in the maps and averaged data that corresponded to abrupt changes in topography (SPM tip encountering surface particle or electrode edge) were removed manually.

Conflict of Interest: The authors declare no competing financial interest.

Acknowledgment. This research was conducted at the Center for Nanophase Materials Sciences, which is sponsored at Oak Ridge National Laboratory by the Scientific User Facilities Division, Office of Basic Energy Sciences, U.S. Department of Energy. The work in National Chiao Tung University was supported by the National Science Council of Republic of China (under Contract No. NSC-101-2119-M-009-003-MY2), Ministry of Education (Grant No. MOE-ATU 101W961), and Center for Interdisciplinary Science at National Chiao Tung University.

Supporting Information Available: Data on the variation of the calibration coefficient over distance and in time as measured by tr-KPFM and band excitation open-loop KPFM are presented. This material is available free of charge *via* the Internet at http://pubs.acs.org.

REFERENCES AND NOTES

1. Kharton, V. V.; Marques, F. M. B.; Atkinson, A. Transport Properties of Solid Oxide Electrolyte Ceramics: A Brief Review. *Solid State Ionics* **2004**, *174*, 135–149.
2. Bagotsky, V. S. *Fuel Cells: Problems and Solutions*; Wiley: New York, 2009.
3. Tarascon, J. M.; Armand, M. Issues and Challenges Facing Rechargeable Lithium Batteries. *Nature* **2001**, *414*, 359–367.
4. Goodenough, J. B.; Kim, Y. Challenges for Rechargeable Li Batteries. *Chem. Mater.* **2010**, *22*, 587–603.
5. Kraytsberg, A.; Ein-Eli, Y. Review on Li-Air Batteries—Opportunities, Limitations and Perspective. *J. Power Sources* **2011**, *196*, 886–893.
6. Adler, S. B. Factors Governing Oxygen Reduction in Solid Oxide Fuel Cell Cathodes. *Chem. Rev.* **2004**, *104*, 4791–4843.
7. Sawa, A. Resistive Switching in Transition Metal Oxides. *Mater. Today* **2008**, *11*, 28–36.
8. *Nanoelectronics and Information Technology*; Wiley-VCH: Berlin, 2012; p 1040.
9. Waser, R.; Aono, M. Nanoionics-Based Resistive Switching Memories. *Nat. Mater.* **2007**, *6*, 833–840.
10. Strukov, D. B.; Snider, G. S.; Stewart, D. R.; Williams, R. S. The Missing Memristor Found. *Nature* **2008**, *453*, 80–83.
11. Likharev, K. K. Hybrid CMOS/Nanoelectronic Circuits: Opportunities and Challenges. *J. Nanoelectron. Optoelectron.* **2008**, *3*, 203–230.
12. *Tutorials in Electrochemical Technology: Impedance Spectroscopy*; The Electrochemical Society: Salem, MA, 2008; Vol. 13, p 171.
13. Barsoukov, E.; Macdonald, J. R. *Impedance Spectroscopy: Theory, Experiment, and Applications*; John Wiley & Sons: Hoboken, NJ, 2005; p 608.
14. Shao, R.; Kalinin, S. V.; Bonnell, D. A. Local Impedance Imaging and Spectroscopy of Polycrystalline ZnO Using Contact Atomic Force Microscopy. *Appl. Phys. Lett.* **2003**, *82*, 1869–1871.
15. O'Hayre, R.; Lee, M.; Prinz, F. B. Ionic and Electronic Impedance Imaging Using Atomic Force Microscopy. *J. Appl. Phys.* **2004**, *95*, 8382–8392.
16. Rozler, M.; Beasley, M. R. Design and Performance of a Practical Variable-Temperature Scanning Tunneling Potentiometry System. *Rev. Sci. Instrum.* **2008**, *79*, 073904-1-13.
17. Muralt, P.; Meier, H.; Pohl, D. W.; Salemink, H. W. M. Scanning Tunneling Microscopy and Potentiometry on a Semiconductor Heterojunction. *Appl. Phys. Lett.* **1987**, *50*, 1352–1354.
18. Kuntze, S. B.; Ban, D.; Sargent, E. H.; Dixon-Warren, S. J.; White, J. K.; Hinzer, K. Electrical Scanning Probe Microscopy: Investigating the Inner Workings of Electronic and Optoelectronic Devices. *Crit. Rev. Solid State Mater. Sci.* **2005**, *30*, 71–124.
19. Shockley, W.; Hooper, W. W.; Queisser, H. J.; Schroen, W. Mobile Electric Charges on Insulating Oxides with Application to Oxide Covered Silicon P-N Junctions. *Surf. Sci.* **1964**, *2*, 277–287.
20. Schlegel, E. S.; Schnable, G. L.; Schwarz, R. F.; Spratt, J. P. Behavior of Surface Ions on Semiconductor Devices. *IEEE Trans. Electron Devices* **1968**, *ED15*, 973–977.
21. Poehlsen, T.; Fretwurst, E.; Klanner, R.; Schuwalow, S.; Schwandt, J.; Zhang, J. G. Charge Losses in Segmented Silicon Sensors at the $Si-SiO_2$ Interface. *Nucl. Instrum. Methods Phys. Res., Sect. A* **2013**, *700*, 22–39.
22. Kiselev, I.; Sommer, M. Evolution of Potential Distributions during the Charging of Nano-structured Metal Oxide Films in Air As Response to Sudden Voltage Application. *Thin Solid Films* **2010**, *518*, 4533–4536.
23. Kiselev, I.; Sommer, M.; Sysoev, V. V.; Skorokhodov, S. L. Electric Field Induced Dynamics of Charged Species in Metal Oxide Devices: Diffusion Equation Analysis. *Phys. Status Solidi A* **2011**, *208*, 2889–2899.
24. Liscio, A.; Palermo, V.; Samorì, P. Nanoscale Quantitative Measurement of the Potential of Charged Nanostructures by Electrostatic and Kelvin Probe Force Microscopy: Unraveling Electronic Processes in Complex Materials. *Acc. Chem. Res.* **2010**, *43*, 541–550.
25. Huang, H.; Wang, H.; Zhang, J.; Yan, D. Surface Potential Images of Polycrystalline Organic Semiconductors Obtained by Kelvin Probe Force Microscopy. *Appl. Phys. A: Mater. Sci. Process.* **2009**, *95*, 125–130.
26. Sadewasser, S.; Glatzel, T. *Kelvin Probe Force Microscopy: Measuring and Compensating Electrostatic Forces*; Springer-Verlag: New York, 2012; p 331.
27. Melitz, W.; Shen, J.; Kummel, A. C.; Lee, S. Kelvin Probe Force Microscopy and Its Application. *Surf. Sci. Rep.* **2011**, *66*, 1–27.
28. Kalinin, S. V.; Bonnell, D. A. Local Potential and Polarization Screening on Ferroelectric Surfaces. *Phys. Rev. B* **2001**, *63*, 125411–125424.
29. Kalinin, S. V.; Bonnell, D. A. Scanning Impedance Microscopy of an Active Schottky Barrier Diode. *J. Appl. Phys.* **2002**, *91*, 832–839.
30. Coffey, D. C.; Ginger, D. S. Time-Resolved Electrostatic Force Microscopy of Polymer Solar Cells. *Nat. Mater.* **2006**, *5*, 735–740.
31. Jiang, Y.; Qi, Q.; Wang, R.; Zhang, J.; Xue, Q.; Wang, C.; Jiang, C.; Qiu, X. Direct Observation and Measurement of Mobile Charge Carriers in a Monolayer Organic Semiconductor on a Dielectric Substrate. *ACS Nano* **2011**, *5*, 6195–6201.
32. Li, X.; Kadashchuk, A.; Fishchuk, I. I.; Smaal, W. T. T.; Gelinck, G.; Broer, D. J.; Genoe, J.; Heremans, P.; Baessler, H. Electric Field Confinement Effect on Charge Transport in Organic Field-Effect Transistors. *Phys. Rev. Lett.* **2012**, *108*, 066601–066605.
33. Sciascia, C.; Celebrano, M.; Binda, M.; Natali, D.; Lanzani, G.; Cabanillas-Gonzalez, J. R. Electric Field and Charge Distribution Imaging with Sub-micron Resolution in an Organic Thin-Film Transistor. *Org. Electron.* **2012**, *13*, 66–70.
34. Pingree, L. S. C.; Rodovsky, D. B.; Coffey, D. C.; Bartholomew, G. P.; Ginger, D. S. Scanning Kelvin Probe Imaging of the Potential Profiles in Fixed and Dynamic Planar Lecs. *J. Am. Chem. Soc.* **2007**, *129*, 15903–15910.
35. Laboriante, I.; Farrokhzad, N.; Fisch, M.; Shavezipur, M.; Carraro, C.; Maboudian, R.; Bai, Q.; Liu, M. Z.; Hoen, S. Charging and Discharging Behavior in Dielectric-Coated Mems Electrodes Probed by Kelvin Probe Force Microscopy. *J. Micromech. Microeng.* **2012**, *22*, 065031–065039.
36. Belarni, A.; Lamhamdi, M.; Pons, P.; Boudou, L.; Guastavino, J.; Segui, Y.; Papaioannou, G.; Plana, R. Kelvin Probe Microscopy for Reliability Investigation of RF-MEMS Capacitive Switches. *Microelectron. Reliab.* **2008**, *48*, 1232–1236.
37. Kalinin, S. V.; Shin, J.; Jesse, S.; Geohegan, D.; Baddorf, A. P.; Lilach, Y.; Moskovits, M.; Kolmakov, A. Electronic Transport Imaging in a Multiwire SnO_2 Chemical Field-Effect Transistor Device. *J. Appl. Phys.* **2005**, *98*, 044503–044508.
38. Andringa, A.-M.; Roelofs, W. S. C.; Sommer, M.; Thelakkat, M.; Kemerink, M.; de Leeuw, D. M. Localizing Trapped Charge Carriers in NO_2 Sensors Based on Organic Field-Effect Transistors. *Appl. Phys. Lett.* **2012**, *101*, 153302–153308.
39. Kolmakov, A.; Lanke, U.; Karam, R.; Shin, J.; Jesse, S.; Kalinin, S. V. Application of Spectromicroscopy Tools To Explore Local Origins of Sensor Activity in Quasi-1D Oxide Nanostructures. *Nanotechnology* **2006**, *17*, 4014–4018.
40. Kalinin, S. V.; Shao, R.; Bonnell, D. A. Local Phenomena in Oxides by Advanced Scanning Probe Microscopy. *J. Am. Ceram. Soc.* **2005**, *88*, 1077–1098.
41. Huey, B. D.; Bonnell, D. A. Spatially Localized Dynamic Properties of Individual Interfaces in Semiconducting Oxides. *Appl. Phys. Lett.* **2000**, *76*, 1012–1014.
42. Suzuki, K.; Okamoto, T.; Kondo, H.; Tanaka, N.; Ando, A. Insulation Degradation Behavior of Multilayer Ceramic Capacitors Clarified by Kelvin Probe Force Microscopy under Ultra-high Vacuum. *J. Appl. Phys.* **2013**, *113*, 064103–064103.
43. Kalinin, S. V.; Suchomel, M. R.; Davies, P. K.; Bonnell, D. A. Potential and Impedance Imaging of Polycrystalline $BiFeO_3$ Ceramics. *J. Am. Ceram. Soc.* **2002**, *85*, 3011–3017.
44. Shin, J.; Meunier, V.; Baddorf, A. P.; Kalinin, S. V. Nonlinear Transport Imaging by Scanning Impedance Microscopy. *Appl. Phys. Lett.* **2004**, *85*, 4240–4242.

45. Kalinin, S. V.; Shin, J.; Veith, G. M.; Baddorf, A. P.; Lobanov, M. V.; Runge, H.; Greenblatt, M. Real Space Imaging of the Microscopic Origins of the Ultrahigh Dielectric Constant in Polycrystalline $CaCu_3Ti_4O_{12}$. *Appl. Phys. Lett.* **2005**, *86*, 102902–102905.
46. Rodriguez, B. J.; Jesse, S.; Meunier, V.; Kalinin, S. V. Scanning Frequency Mixing Microscopy of High-Frequency Transport Behavior at Electroactive Interfaces. *Appl. Phys. Lett.* **2006**, *88*, 143128–143131.
47. Kalinin, S. V.; Bonnell, D. A. Surface Potential at Surface-Interface Junctions in $SrTiO_3$ Bicrystals. *Phys. Rev. B* **2000**, *62*, 10419–10430.
48. Brunel, D.; Mayer, A.; Melin, T. Imaging the Operation of a Carbon Nanotube Charge Sensor at the Nanoscale. *ACS Nano* **2010**, *4*, 5978–5984.
49. Kalinin, S. V.; Bonnell, D. A.; Freitag, M.; Johnson, A. T. Carbon Nanotubes as a Tip Calibration Standard for Electrostatic Scanning Probe Microscopies. *Appl. Phys. Lett.* **2002**, *81*, 754–756.
50. Kalinin, S. V.; Bonnell, D. A. Screening Phenomena on Oxide Surfaces and Its Implications for Local Electrostatic and Transport Measurements. *Nano Lett.* **2004**, *4*, 555–560.
51. Yang, C. H.; Seidel, J.; Kim, S. Y.; Rossen, P. B.; Yu, P.; Gajek, M.; Chu, Y. H.; Martin, L. W.; Holcomb, M. B.; He, Q.; *et al.* Electric Modulation of Conduction in Multiferroic Ca-Doped $BiFeO_3$ Films. *Nat. Mater.* **2009**, *8*, 485–493.
52. Seidel, J.; Luo, W.; Suresha, S. J.; Nguyen, P. K.; Lee, A. S.; Kim, S. Y.; Yang, C. H.; Pennycook, S. J.; Pantelides, S. T.; Scott, J. F.; *et al.* Prominent Electrochromism through Vacancy-Order Melting in a Complex Oxide. *Nat. Commun.* **2012**, *3*, 799–805.
53. Bharathi, K. K.; Lee, W.-M.; Sung, J. H.; Lim, J. S.; Kim, S. J.; Chu, K.; Park, J. W.; Song, J. H.; Jo, M.-H.; Yang, C.-H. Detection of Electrically Formed Photosensitive Area in Ca-Doped $BiFeO_3$ Thin Films. *Appl. Phys. Lett.* **2013**, *102*, 012908–012911.
54. Wang, R. V.; Fong, D. D.; Jiang, F.; Highland, M. J.; Fuoss, P. H.; Thompson, C.; Kolpak, A. M.; Eastman, J. A.; Streiffer, S. K.; Rappe, A. M.; *et al.* Reversible Chemical Switching of a Ferroelectric Film. *Phys. Rev. Lett.* **2009**, *102*, 047601–047604.
55. Fong, D. D.; Kolpak, A. M.; Eastman, J. A.; Streiffer, S. K.; Fuoss, P. H.; Stephenson, G. B.; Thompson, C.; Kim, D. M.; Choi, K. J.; Eom, C. B.; *et al.* Stabilization of Monodomain Polarization in Ultrathin $PbTiO_3$ Films. *Phys. Rev. Lett.* **2006**, *96*, 127601–127604.
56. Kalinin, S. V.; Bonnell, D. A. Local Potential and Polarization Screening on Ferroelectric Surfaces. *Phys. Rev. B* **2001**, *63*, 125411–125424.
57. Kalinin, S. V.; Johnson, C. Y.; Bonnell, D. A. Domain Polarity and Temperature Induced Potential Inversion on the $BaTiO_3$(100) Surface. *J. Appl. Phys.* **2002**, *91*, 3816–3823.
58. Barsan, N.; Koziej, D.; Weimar, U. Metal Oxide-Based Gas Sensor Research: How To? *Sens. Actuators, B* **2007**, *121*, 18–35.
59. Belaidi, S.; Girard, P.; Leveque, G. Electrostatic Forces Acting on the Tip in Atomic Force Microscopy: Modelization and Comparison with Analytic Expressions. *J. Appl. Phys.* **1997**, *81*, 1023–1030.
60. Charrier, D. S. H.; Kemerink, M.; Smalbrugge, B. E.; de Vries, T.; Janssen, R. A. J. Real *versus* Measured Surface Potentials in Scanning Kelvin Probe Microscopy. *ACS Nano* **2008**, *2*, 622–626.
61. Bayerl, D. J.; Wang, X. Three-Dimensional Kelvin Probe Microscopy for Characterizing In-Plane Piezoelectric Potential of Laterally Deflected ZnO Micro-/Nanowires. *Adv. Funct. Mater.* **2012**, *22*, 652–660.
62. Strassburg, E.; Boag, A.; Rosenwaks, Y. Reconstruction of Electrostatic Force Microscopy Images. *Rev. Sci. Instrum.* **2005**, *76*, 083705–8.
63. Sadewasser, S.; Glatzel, T.; Shikler, R.; Rosenwaks, Y.; Lux-Steiner, M. C. Resolution of Kelvin Probe Force Microscopy in Ultrahigh Vacuum: Comparison of Experiment and Simulation. *Appl. Surf. Sci.* **2003**, *210*, 32–36.
64. Liscio, A.; Palermo, V.; Samori, P. Nanoscale Quantitative Measurement of the Potential of Charged Nanostructures by Electrostatic and Kelvin Probe Force Microscopy: Unraveling Electronic Processes in Complex Materials. *Acc. Chem. Res.* **2010**, *43*, 541–550.
65. Kalinin, S. V.; Rodriguez, B. J.; Jesse, S.; Morozovska, A. N.; Bokov, A. A.; Ye, Z. G. Spatial Distribution of Relaxation Behavior on the Surface of a Ferroelectric Relaxor in the Ergodic Phase. *Appl. Phys. Lett.* **2009**, *95*, 142902–142905.
66. Kumar, A.; Ehara, Y.; Wada, A.; Funakubo, H.; Griggio, F.; Trolier-McKinstry, S.; Jesse, S.; Kalinin, S. V. Dynamic Piezoresponse Force Microscopy: Spatially Resolved Probing of Polarization Dynamics in Time and Voltage Domains. *J. Appl. Phys.* **2012**, *112*, 052021–052024.
67. Kumar, A.; Ovchinnikov, O. S.; Funakubo, H.; Jesse, S.; Kalinin, S. V. Real-Space Mapping of Dynamic Phenomena during Hysteresis Loop Measurements: Dynamic Switching Spectroscopy Piezoresponse Force Microscopy. *Appl. Phys. Lett.* **2011**, *98*, 202903–202905.
68. Pines, E.; Huppert, D.; Agmon, N. Germinate Recombination in Excited-State Proton-Transfer Reactions—Numerical Solution of the Debye-Smoluchowski Equation with Back-reaction and Comparison with Experimental Results. *J. Chem. Phys.* **1988**, *88*, 5620–5630.
69. Chen, H.; Voth, G. A.; Agmon, N. Kinetics of Proton Migration in Liquid Water. *J. Phys. Chem. B* **2010**, *114*, 333–339.
70. Ho, C.; Raistrick, I. D.; Huggins, R. A. Application of Ac Techniques to the Study of Lithium Diffusion in Tungsten Trioxide Thin Films. *J. Electrochem. Soc.* **1980**, *127*, 343–350.
71. Weppner, W.; Huggins, R. A. Electrochemical Methods for Determining Kinetic Properties of Solids. *Annu. Rev. Mater. Sci.* **1978**, *8*, 269–311.
72. Weppner, W.; Huggins, R. A. Determination of Kinetic Parameters of Mixed Conducting Electrodes and Application to System Li_3Sb. *J. Electrochem. Soc.* **1977**, *124*, 1569–1578.
73. Jesse, S.; Kalinin, S. V. Band Excitation in Scanning Probe Microscopy: Sines of Change. *J. Phys. D: Appl. Phys.* **2011**, *44*, 464006–464010.
74. Jesse, S.; Kalinin, S. V.; Proksch, R.; Baddorf, A. P.; Rodriguez, B. J. The Band Excitation Method in Scanning Probe Microscopy for Rapid Mapping of Energy Dissipation on the Nanoscale. *Nanotechnology* **2007**, *18*, 435503–435510.
75. Guo, S.; Kalinin, S. V.; Jesse, S. Open-Loop Band Excitation Kelvin Probe Force Microscopy. *Nanotechnology* **2012**, *23*, 125704–125713.
76. Guo, S.; Kalinin, S. V.; Jesse, S. Half-Harmonic Kelvin Probe Force Microscopy with Transfer Function Correction. *Appl. Phys. Lett.* **2012**, *100*, 063118–0631122.
77. Giridharagopal, R.; Rayermann, G. E.; Shao, G.; Moore, D. T.; Reid, O. G.; Tillack, A. F.; Masiello, D. J.; Ginger, D. S. Submicrosecond Time Resolution Atomic Force Microscopy for Probing Nanoscale Dynamics. *Nano Lett.* **2012**, *12*, 893–898.